# Dilated cardiomyopathy mutation in beta-cardiac myosin enhances actin activation of the power stroke and phosphate release

Skylar M. L. Bodt [ID][a], Jinghua Ge [ID][a], Wen Ma [ID][b], David V. Rasicci [ID][a,c], Rohini Desetty [ID][a], J. Andrew McCammon [ID][d] and Christopher M. Yengo [ID][a,*]

[a]Department of Cellular and Molecular Physiology, Pennsylvania State University College of Medicine, 500 University Dr, Hershey, PA 17033, USA
[b]Department of Physics, University of Vermont, 149 Beaumont Avenue, Burlington, VT 05405, USA
[c]Department of Pathology, Anatomy, and Laboratory Medicine, West Virginia University School of Medicine, 64 Medical Center Dr, Morgantown, WV 26506, USA
[d]Department of Chemistry and Biochemistry, University of California San Diego, 9500 Gilman Dr, La Jolla, CA 92093, USA
*To whom correspondence should be addressed: Email: cmy11@psu.edu
**Edited By** Peter Fratzl

## Abstract

Inherited mutations in human beta-cardiac myosin (M2β) can lead to severe forms of heart failure. The E525K mutation in M2β is associated with dilated cardiomyopathy (DCM) and was found to stabilize the interacting heads motif (IHM) and autoinhibited super-relaxed (SRX) state in dimeric heavy meromyosin. However, in monomeric M2β subfragment 1 (S1) we found that E525K enhances (threefold) the maximum steady-state actin-activated ATPase activity ($k_{cat}$) and decreases (eightfold) the actin concentration at which ATPase is one-half maximal ($K_{ATPase}$). We also found a twofold to fourfold increase in the actin-activated power stroke and phosphate release rate constants at 30 μM actin, which overall enhanced the duty ratio threefold. Loaded motility assays revealed that the enhanced intrinsic motor activity translates to increased ensemble force in M2β S1. Glutamate 525, located near the actin binding region in the so-called activation loop, is highly conserved and predicted to form a salt bridge with another conserved residue (lysine 484) in the relay helix. Enhanced sampling molecular dynamics simulations predict that the charge reversal mutation disrupts the E525-K484 salt bridge, inducing conformations with a more flexible relay helix and a wide phosphate release tunnel. Our results highlight a highly conserved allosteric pathway associated with actin activation of the power stroke and phosphate release and suggest an important feature of the autoinhibited IHM is to prevent this region of myosin from interacting with actin. The ability of the E525K mutation to stabilize the IHM likely overrides the enhanced intrinsic motor properties, which may be key to triggering DCM pathogenesis.

**Keywords:** myosin, actin, heart failure, muscle contraction, enzymology

---

**Significance Statement**

Heart disease can be caused by inherited mutations in beta-cardiac myosin, the molecular motor that powers systolic contraction in the ventricles of the heart. However, it remains unclear how these mutations lead to contractile dysfunction and pathogenic remodeling of the heart. We investigated a unique dilated cardiomyopathy mutation (E525K) that dramatically stabilizes the autoinhibited state while enhancing intrinsic motor function. Thus, we examined how this mutation impacts transient kinetic steps of the ATPase cycle, motile properties, and structural changes associated with the power stroke and phosphate release. Our results provide a kinetic and structural basis for how beta-cardiac myosin mutations may disrupt molecular-level contractile function in complex ways, which may inform the development of targeted therapeutics.

---

## Introduction

Human beta-cardiac myosin (M2β) is the molecular motor that powers systolic contraction within the heart by utilizing a conserved actomyosin ATPase mechanism (Fig. 1) (1, 2). It is well established that generation of force and power in cardiac muscle is determined by the recruitment of myosin motors during the

systolic rise of calcium. During cardiac systole, cytoplasmic calcium binds troponin-C causing a conformational shift in tropomyosin that allows myosin to bind actin (3). Myosin heads drive contraction according to the sliding filament theory by harnessing mechanical energy from ATP hydrolysis to initiate the force generating power stroke (4). More recently, it has been revealed that

**Fig. 1.** Structure of M2β S1 highlighting the E525 residue and the actomyosin ATPase cycle. A) The key domains of myosin, location of E525 at the base of the activation loop within the lower 50 kDa domain, and other structural elements (e.g. switch I and switch II) of the cardiac myosin motor are highlighted (PDB 5N69). B) The active site demonstrating the role of switch I and II in coordinating the gamma phosphate of ATP. C) The E525 residue and its proximity to the K484 residue on the relay helix. D) The kinetic scheme used to examine the key steps in the actomyosin ATPase cycle.

muscle myosins can occupy an autoinhibited state called the super relaxed (SRX) state with 10-fold slower ATP turnover that plays an important role in thick filament regulation (5–9). Reports have found correlations between this SRX state and the interacting heads motif (IHM), a conformation where myosin heads fold back on a region of the tail (subfragment 2) and interact with each other (10). The intricate balance between the force generating mechanism and autoinhibition of the thick filament remains elusive (11). Examining these biochemical and structural events is crucial for understanding the system of energy transduction and regulation in myosin.

Cardiomyopathy is a disease of the heart muscle that results in impaired pump function and frequently leads to heart failure. The two most prevalent genetically induced cardiomyopathies, hypertrophic cardiomyopathy (HCM) and dilated cardiomyopathy (DCM), have been linked to mutations in human beta-cardiac myosin, encoded by *MYH7* (12). HCM presents clinically as an increase in hypertrophy and ventricle wall thickening, often causing diastolic dysfunction, myofilament disarray, and fibrosis. In contrast, DCM, the second most common cause of heart failure, is characterized by wall thinning, left ventricular dilation, and a dramatic decrease in ejection fraction. Previous HCM and DCM cardiomyopathy *MYH7* variant studies have been successful in contributing to our understanding of how impaired cardiac myosin impacts disease pathogenesis. These studies have resulted in small molecule therapeutics, such as Mavacamten and Omecamtiv Mecarbil (13–17). However, the complex ramifications of myosin mutations on motor function are not entirely understood. For example, the leading hypothesis suggests that beta-cardiac myosin mutations that are "gain of function" are associated with HCM, whereas "loss of function" are associated with

DCM (18). However, exceptions have been identified, leaving room for debate within the field (10, 19, 20).

One intriguing feature of the myosin ATPase mechanism is that actin binding dramatically accelerates ATPase activity, in some cases by several orders of magnitude (21, 22). This feature requires a precise structural mechanism that allosterically connects the actin binding region with the active site. The conserved myosin motor domain is composed of four subdomains, the upper and lower 50 kDa domains, the N-terminal domain, and the converter/lever arm domain (Fig. 1A) (2). In the current paper, we focus on a region of the lower 50 kDa domain, known as the activation loop, which is thought to be crucial for triggering actin activation of ATPase activity (Fig. 1B & C). Previously, we studied the DCM mutation (E525K) located in the conserved activation loop (see alignment Fig. S1) and found that it dramatically enhanced actin-activated ATPase activity and the apparent affinity for actin (10). In addition, we found that this mutation dramatically stabilized the autoinhibited IHM and the SRX states even at physiological ionic strength (10, 23). We hypothesized that this region of myosin was crucial for stabilizing the electrostatic interactions that form the IHM, thus regulating the number of active heads in the thick filament. In the present study, we examined the impact of the E525K mutation on the transient kinetic steps of the ATPase cycle which allowed us to precisely determine the ATPase mechanism and the fraction of the ATPase cycle where myosin is in the force generating states (duty ratio). We measured the power stroke rate constant using a FRET sensor of myosin lever arm rotation and performed Gaussian accelerated molecular dynamics simulations to predict structural changes and allosteric pathways. In addition, we investigated the impact of the mutation on the motile and force generating properties of S1 using unloaded

and loaded motility assays. We demonstrate that the mutation uncovers a highly conserved allosteric pathway that is crucial for actin activation of the power stroke and phosphate release. Thus, our work highlights a conserved actin binding motif that can either interact with subfragment 2 (S2) to form the IHM or interact with actin to produce force, making it a major determinant of whether myosin can form an autoinhibited or force generating myosin head.

## Results

### Steady-state actin-activated ATPase activity

In our previous work, we expressed and purified human cardiac myosin subfragment 1 (M2β S1) (see SDS-PAGE in Rasicci et al. (10)) and examined the actomyosin ATPase cycle in MOPS 20 buffer (10 mM MOPS at pH 7.0, 20 mM KCl, 1 mM EGTA, 1 mM MgCl$_2$, 1 mM DTT) (10, 24, 25). In the current study, we used a buffer containing higher Mg$^{2+}$ (4 mM MgCl$_2$) to minimize differences between the mutant and WT that were solely due to differences in Mg$^{2+}$ affinity (26). A lower salt concentration (5 mM KCl) was utilized to allow saturation of the actin-activated ATPase reaction, which is highly sensitive to ionic strength. Therefore, the kinetic experiments were performed in MOPS 5/4 buffer (10 mM MOPS at pH 7.0, 5 mM KCl, 1 mM EGTA, 4 mM MgCl$_2$, 1 mM DTT). The actin-activated ATPase activity of M2β S1 WT and E525K was examined in three independent protein preparations and the average ATPase, at each actin concentration, was plotted as a function of actin concentration and fit to the Michaelis–Menten equation to determine the maximum rate of steady-state actin-activated ATPase activity ($k_{cat}$) and the concentration at which ATPase activity is one-half maximal ($K_{ATPase}$) (Fig. 2A) (27). Our results reveal a 2.7-fold increase in the E525K $k_{cat}$ (10.06 ± 0.03 s$^{-1}$) and a 7.6-fold decrease in E525K $K_{ATPase}$ (3.99 ± 0.59 μM) when compared to the $k_{cat}$ and $K_{ATPase}$ values of the WT construct, respectively (3.76 ± 0.53 s$^{-1}$, 30.33 ± 9.3 μM) (Table 1). We also determined that the ATPase activity without actin, $v_0$, was enhanced twofold by the mutation (WT, 0.02 ± 0.01 s$^{-1}$; E525K, 0.04 ± 0.01 s$^{-1}$) (Table 1). Single ATP turnover measurements were also utilized to examine the ATPase activity without actin (Fig. 2B). Myosin was first incubated with mant-labeled ATP and subsequently mixed with a high concentration (1 mM) of dark ATP. We found that the slow phase representing the SRX state was a small fraction of the fluorescence transients in both WT and E525K (~5%) (Table 1). The rate constant for the fast phase, referred to as the disordered relaxed (DRX) state, was twofold faster in E525K compared with WT M2β S1 (Table 1).

### Impact of E525K on transient kinetic steps of the ATPase cycle

We investigated the impact of the E525K mutation on the predominant steps of the actomyosin ATPase cycle. The results were interpreted in the context of a simplified kinetic scheme of the actomyosin ATPase cycle (Fig. 1D) (1, 11). The equilibrium constants in this scheme, each with associated forward (right) and reverse (left) rate constants (not shown for simplicity), are referred to throughout the manuscript.

The ATP binding and hydrolysis steps were measured by monitoring the tryptophan fluorescence enhancement that occurs when M2β S1 (1 μM) was mixed with varying concentrations of ATP. Fluorescence transients were best fit to a double exponential function and the rate constants were plotted as a function of ATP concentration (Fig. S2A & C). The fast phase rate constants were
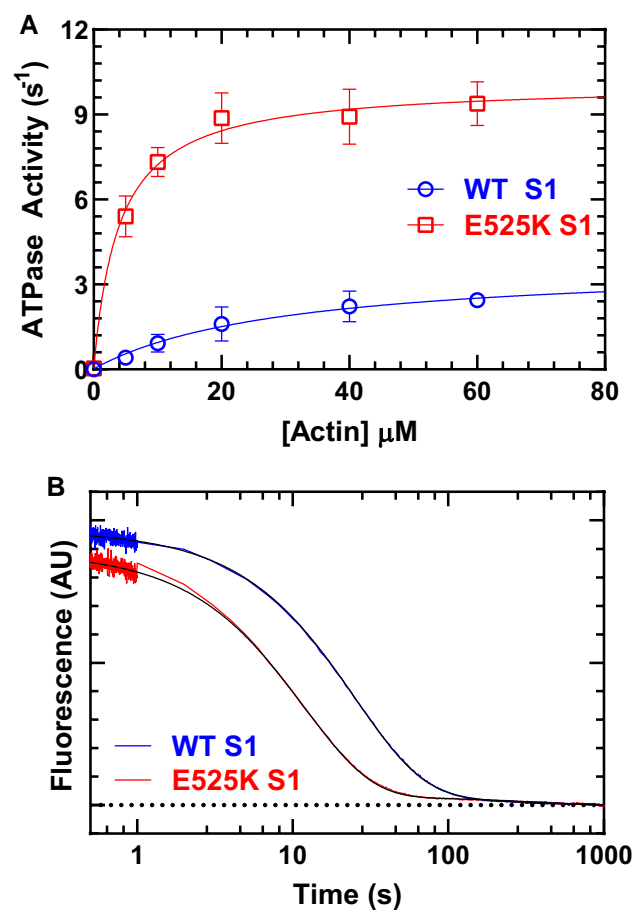
**Fig. 2.** Steady-state ATPase kinetics. A) The actin-activated ATPase activity of purified M2β S1 WT and E525K was determined as a function of actin concentration. The data points represent the average ± SD from five protein preparations. B) Turnover of mant-ATP by M2β S1 WT and E525K was examined for 1000 s after (0.25 μM) myosin was preincubated with mant-ATP (1 μM) for ~30 s and then mixed with saturating unlabeled ATP (2 mM). Fluorescence transients were best fit to a double exponential function. Some error bars are not visible because they are smaller than the symbols (e.g. WT @ 60 μM actin).

**Table 1.** Summary of steady-state kinetic measurements.

| Kinetic Parameter | Method | WT S1 | E525K S1 |
|---|---|---|---|
| $v_0$ (s$^{-1}$), N = 3 | NADH Assay | 0.020 ± 0.006 | *0.043 ± 0.010 |
| $k_{cat}$ (s$^{-1}$), N = 5 | NADH Assay | 3.76 ± 0.53 | *10.06 ± 0.30 |
| $K_{ATPase}$ (μM), N = 5 | NADH Assay | 30.33 ± 9.29 | *3.99 ± 0.59 |
| SRX rate (s$^{-1}$), N = 4 | mant-ATP Single Turnover | 0.0041 ± 0.0025 | 0.0027 ± 0.0023 |
| DRX rate (s$^{-1}$), N = 4 | mant-ATP Single Turnover | 0.038 ± 0.003 | *0.072 ± 0.022 |
| DRX fraction, N = 4 | mant-ATP Single Turnover | 0.95 ± 0.01 | 0.94 ± 0.02 |

*P < 0.05. Errors reported are standard deviation, except for $K_{ATPase}$ and $k_{cat}$ which are standard error of the fits.

dependent on ATP concentration and were fit to a hyperbolic function to determine the maximum rate of ATP hydrolysis, $k_{+H}+k_{-H}$ (s$^{-1}$), and dependence on ATP concentration, $K_{0.5}$ (μM) (Fig. S2B). E525K showed a slightly reduced maximum rate of ATP hydrolysis (100.4 ± 3.2 s$^{-1}$) compared to WT (127.9 ± 4.2 s$^{-1}$)

**Table 2.** Summary of transient kinetic measurements.

| Kinetic Step | Method | Rate/equilibrium constant | WT S1 | E525K S1 |
|---|---|---|---|---|
| ATP binding to M | Tryp. Fluor | $K_{1T}k_{2T}$ ($\mu M^{-1}s^{-1}$) | $3.5 \pm 0.2$ | $*2.7 \pm 0.2$ |
| $N = 3$ | | $K_{0.5}$ ($\mu M$) | $21.6 \pm 2.7$ | $20.9 \pm 2.6$ |
| ATP hydrolysis | Tryp. Fluor | $k_{+H} + k_{-H}$ ($s^{-1}$) | $127.9 \pm 4.2$ | $*100.4 \pm 3.2$ |
| $N = 3$ | | | | |
| ATP binding to AM | Pyrene Actin | $K'_{1T}k'_{2T}$ ($\mu M^{-1}s^{-1}$) | $6.8 \pm 0.5$ | $8.0 \pm 0.8$ |
| $N = 5$ | | | | |
| Dissociation of AM by ATP $N = 4$ | Pyrene Actin | $k'_{+2T}$ ($s^{-1}$) | $827.8 \pm 111.8$ | $*1993 \pm 212.4$ |
| | | $K_{0.5}$ ($\mu M$) | $99.8 \pm 22.6$ | $212.4 \pm 99.1$ |
| Power Stroke (fast) | FRET | $k'_{+PW}$ ($s^{-1}$) | $10.7 \pm 6.8$ | $*43.7 \pm 8.0$ |
| @ 30 $\mu M$ actin, $N = 3$ | | $K_{0.5}$ ($\mu M$) | | $17.4 \pm 9.8$ |
| Power Stroke (slow) | FRET | $k'_{+PW}$ (slow) ($s^{-1}$) | $1.0 \pm 0.3$ | $2.3 \pm 1.7$ |
| @ 30 $\mu M$ actin, $N = 4–5$ reps | | | | |
| Pi release (fast), | MDCC-PBP | $k'_{+Pi}$ ($s^{-1}$) | $19.8 \pm 6.1$ | $*45.2 \pm 15.0$ |
| @ 30 $\mu M$ actin, $N = 3$ | | $K_{0.5}$ ($\mu M$) | | $4.0 \pm 2.2$ |
| Pi release (slow) | MDCC-PBP | $k'_{+Pi}$ (slow) ($s^{-1}$) | $2.4 \pm 0.6$ | $2.8 \pm 0.3$ |
| $N = 3$ | | $K_{0.5}$ ($\mu M$) | $12.8 \pm 7.8$ | $1.0 \pm 0.9$ |
| ADP dissociation from AM | Pyrene Actin | $k'_{+ADP}$ ($s^{-1}$) | $116.5 \pm 16.0$ | $114.5 \pm 12.1$ |
| $N = 4–7$ | mant-ADP | $k'_{+ADP}$ ($s^{-1}$) | $291.4 \pm 27.0$ | $*327.9 \pm 20.2$ |

*$P < 0.05$. Errors reported are standard error of the fit, except for Power stroke ($k'_{+PW}$), Pi release ($k'_{+Pi}$), ADP dissociation ($k'_{+ADP}$) which are standard deviation.

while $K_{0.5}$ values were similar for both constructs (WT, $21.6 \pm 2.7$ µM; E525K, $20.9 \pm 2.6$ µM) (Table 2). The second-order rate constant for ATP binding to myosin, $K_{1T}k_{2T}$ ($\mu M^{-1}s^{-1}$), was determined by the linear dependence of the fast phase on ATP concentration at lower concentrations of ATP, which was similar for both constructs (WT, $3.5 \pm 0.2$ $\mu M^{-1}s^{-1}$; E525K, $2.7 \pm 0.2$ $\mu M^{-1}s^{-1}$) (Table 2). The rate constant of the slow phase, which represented 10–20% of the fluorescence signal, was independent of ATP concentration and similar in WT and E525K ($\sim 20$ $s^{-1}$).

ATP-induced dissociation from actin was measured by mixing M2β S1 (0.5 µM) complexed with equal molar pyrene labeled actin (0.5 µM) with increasing concentrations of ATP. Fluorescence transients were best fit to a single exponential function and the rate constants were fit to a hyperbolic function to determine the maximum rate of transition into the weakly bound states, $k'_{+2T}$ ($s^{-1}$), and the equilibrium constant for the initial interaction of ATP with actomyosin ($K'_{1T}$) ($k_{obs} = [ATP]k'_{+2T}/([ATP] + K_{0.5})$, where $K_{0.5} = 1/K'_{1T}$) (Fig S3A & C). The E525K mutation enhanced $k'_{+2T}$ ($1993 \pm 212.4$ $s^{-1}$) 2.4-fold compared to WT ($827.8 \pm 111.8$ $s^{-1}$) (Table 2). The second-order rate constant, $K'_{1T}k'_{+2T}$ ($\mu M^{-1}s^{-1}$), determined from the linear fit of the fast phase at lower ATP concentrations, was similar in both constructs (Fig. S3B). The $K_{0.5}$ was not significantly different between constructs (Table 2).

A sequential-mix stopped-flow configuration was used to measure the rate of actin-activated phosphate release. Actin-activated phosphate release was measured by mixing M2β S1 with sub stoichiometric ATP and aging for 10 seconds to allow ATP binding and hydrolysis followed by a second mix with actin in the presence of phosphate-binding protein (final concentrations: 1 uM M2β, 0.9 µM ATP, 4 µM PBP, and 5–30 µM actin). Phosphate release fluorescent transients collected under single turnover conditions were best fit by a 2- or 3-exponential function (Fig. 3). The very slow phase observed in some of phosphate release transients ($\sim 0.1$–$0.3$ $s^{-1}$) was considered to be caused by the reaction in the absence of actin or off pathway intermediates and thus was not included in the actin-activated phosphate release analysis discussed hereafter. The maximum rate of the slow phase, $k'_{+Pi}$ (slow) ($s^{-1}$), was similar for both the WT and mutant (WT, $2.4 \pm 0.6$ $s^{-1}$; E525K, $2.8 \pm 0.3$ $s^{-1}$) (Fig. 3B, Table 2). The mutant does demonstrate an enhanced actin dependence of $k'_{+Pi}$ (slow), as it is able to plateau at a much lower actin concentration. The E525K construct produced a 2.3-fold increase in the

fast phase of actin-activated phosphate release, $k'_{+Pi}$ (fast) ($s^{-1}$), compared to WT at 30 µM actin (WT, $19.8 \pm 6.1$ $s^{-1}$; E525K, $45.2 \pm 15.0$ $s^{-1}$) (Fig. 3A, Table 2). The maximum rate of $k'_{+Pi}$ (fast) was found to be $53.5 \pm 7.7$ for the mutant but was not determined for WT. E525K demonstrated an increased relative amplitude of the fast phase while WT was dominated by the slow phase (fast phase relative amplitude; WT, $11 \pm 3\%$; E525K, $67 \pm 5\%$).

We examined the rate constant for ADP release from actomyosin, $k'_{+ADP}$ ($s^{-1}$), by mixing a pyrene actomyosin-ADP complex (0.5 µM actomyosin: 10 µM ADP) with saturating ATP (2 mM) (Fig. S4A). Similar rate constants were observed for WT and E525K (WT, $116.5 \pm 16.0$ $s^{-1}$; E525K, $114.5 \pm 12.1$ $s^{-1}$) (Table 2). The rate constant for ADP release from actomyosin was also calculated using a second method with mant-ADP (Fig. S4B). The actomyosin mant-ADP complex (0.5 µM actomyosin: 10 µM mant-ADP) was mixed with saturated (1 mM) ATP. The rate constants were faster than with unlabeled ADP, as we reported previously (24, 25), and we observed a slight increase with the mutant (WT, $291.4 \pm 27.0$ $s^{-1}$; E525K, $327.9 \pm 20.2$ $s^{-1}$) (Table 2). Also, utilizing mant-ADP we examined the ADP release rate constant in varying buffer conditions containing different concentrations of $MgCl_2$ (Fig. S4C and Table S2), which allowed us to compare to the buffer conditions utilized for in vitro motility assays (see in vitro motility *Results*). We found that E525K was more sensitive to $MgCl_2$ concentrations, displaying a twofold decrease in the ADP release rate constant when comparing 1 and 4 mM $MgCl_2$. The corresponding experiments in the WT construct demonstrated a 12% decrease in the ADP release rate constant.

In a previous study, we employed a FRET approach for measuring the rotation of the lever arm in M2β S1 by monitoring the transition from the pre to post-power stroke states (24). Power stroke FRET was examined by exchanging Alexa488 labeled RLC onto M2β S1 (donor) and then utilizing Cy3-labeled nucleotides bound to the active site as the acceptor. To measure the actin-activated power stroke, M2β S1 A488RLC was mixed with substoichiometric Cy3ATP, aged for 10 seconds to allow for hydrolysis to occur, and then mixed with actin (final concentrations 0.5 µM M2B, 0.45 µM Cy3ATP, and 5–30 µM actin). The traces were best fit to a double exponential function, especially at higher actin concentrations (10, 20, and 30 µM) (Fig. 4). The fast phase of the power stroke measurements was hyperbolically dependent on actin concentration in E525K, which allowed us to determine the maximum
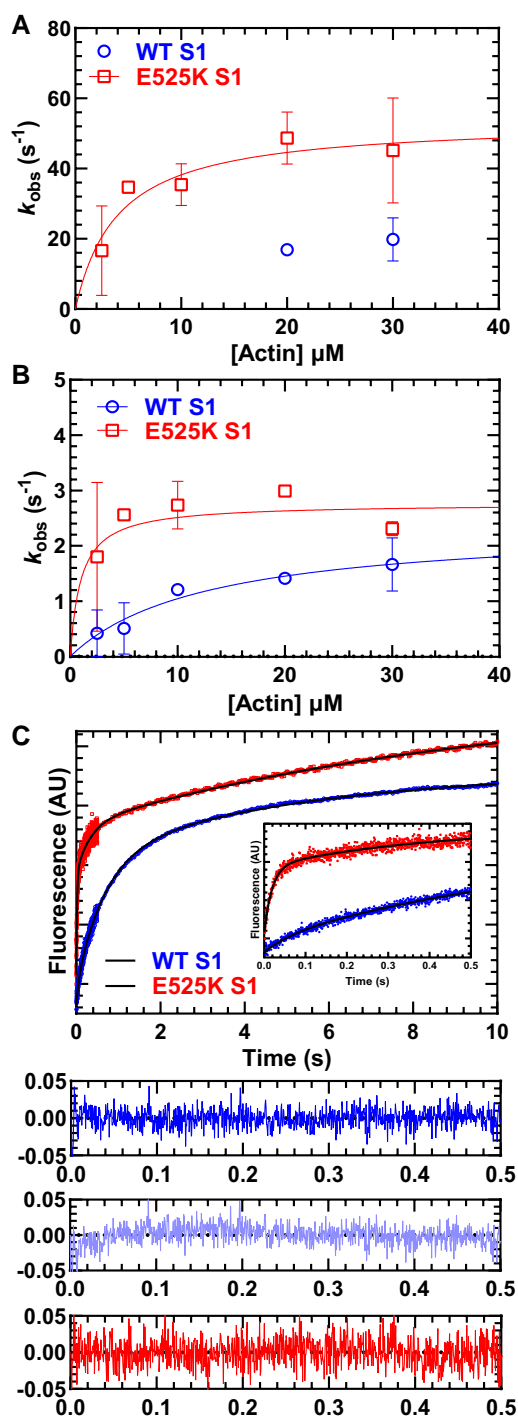
**Fig. 3.** Actin-activated phosphate release. The phosphate-binding protein (MDCC-PBP) was used to monitor the phosphate release step using sequential-mix experiments. M2β S1 was mixed with substoichiometric ATP, aged for 10 s, and then mixed with actin and MDCC-PBP (final concentrations: 1 μM M2B S1, 0.9 μM ATP, 5 μM MDCC-PBP, and 5–30 μM actin). The rate constants of the A) fast and B) slow phases were plotted as a function of actin concentration and fitted to a hyperbolic function. C) Representative fluorescence transients in the presence of 20 μM actin are shown fitted to a three-exponential function. Residuals are shown below panel C, for E525K (red) and WT fitted with a 3-exponential function (dark blue) or 2-exponential function (light blue-without the fast phase shown in panel A). Data points at each actin concentration represent the average ± SD of two experiments from two separate protein preparations, except for 30 μM actin which represents two to three preparations and $N = 5$ replicates for WT and $N = 4$ replicates for E525K. Some error bars are not visible because they are smaller than the symbols.

rate of the power stroke ($k_{+PWS} = 66.9 \pm 18$). In WT M2β S1, we also observed two exponentials in the power stroke transients, but the fast phase rate constant did not saturate in this actin concentration range preventing us from determining the maximum rate. Thus, we report the power stroke rate constant at 30 μM actin to compare the WT and mutant constructs. The E525K mutation increased the fast phase rate, $k'_{PW}$ (fast) (s$^{-1}$), fourfold (WT, $10.7 \pm 6.8$ s$^{-1}$; E525K, $43.7 \pm 8.0$ s$^{-1}$) while the slow phase rate, $k'_{PW}$ (slow) (s$^{-1}$) was not significantly different (WT, $1.0 \pm 0.3$ s$^{-1}$; E525K, $2.3 \pm 1.7$ s$^{-1}$) at 30 μM actin (Table 2). The relative amplitude of the fast phase of the fluorescence transients at 30 μM actin was larger in E525K than WT ($89 \pm 0.01\%$ and $53 \pm 0.16\%$, respectively).

## Kinetic simulations and duty ratio

In order to determine the predominate kinetic pathway of WT and E525K S1, we performed kinetic simulations using the individual rate constants measured, as well as taking into consideration other published studies (Table S1) (24, 25, 28, 29). We favor a model in which myosin proceeds through actin-bound ($K'_H$) and actin-detached ($K_H$) ATP hydrolysis pathways. In addition, the actin-activated power stroke ($K'_{PW}$) occurs prior to the release of phosphate ($K'_{Pi}$). The rate constants for the kinetics steps not measured in the current study were adjusted manually until the simulated data fit best to the experimental data. This model fits reasonably well to the steady-state ATPase (Fig. S5A) as well as the phosphate release (Fig. S5B & C) and power stroke (Fig. S5D & E) rate constants for both the mutant and WT.

The duty ratio at saturating actin concentration was estimated by performing kinetic simulations to determine the fraction of myosin populating the force generating states (AM$^\#$.ADP.Pi and AM.ADP) under steady-state conditions. Using this method, we calculate that the mutant enhances the duty ratio approximately threefold (WT, 0.04; E525K, 0.11).

## Impact of E525K on actin sliding velocity and contractile force

We performed both unloaded and loaded in vitro actin gliding assays with WT and E525K M2β S1. All motility assays were performed at room temperature (~22–23°C) in MOPS 50/1 buffer (10 mM MOPS, pH 7.0, 50 mM KCl, 1 mM EGTA, 1 mM MgCl$_2$, 1 mM DTT). We found MOPS 50/1 to be optimal for minimizing filament breaking (see Fig. S6 and Table S2), which is crucial for performing the loaded motility assay. In MOPS 5/4 buffer, we observed significant filament breaking that was only slightly improved by reducing the MgCl$_2$ to 1 mM. We found that increasing the KCl concentration 10-fold to 50 mM did reduce filament breaking but was improved even more when MgCl$_2$ was reduced to 1 mM (MOPS 50/1) (see supplemental movies S1–S4). The unloaded sliding velocity was about 20% faster in the E525K mutant in MOPS 50/1 buffer, and the increase was consistent over a wide range of densities (Fig. 5A). We fit the density-dependent data to a hyperbolic function to determine the maximum velocity ($V_{MAX}$) and density at which the velocity is one-half maximal ($K_{0.5}$) (Fig. 5; Table 3). The $K_{0.5}$ was shifted twofold lower in the mutant, consistent with an increase in duty ratio. We also performed in vitro motility in the presence of varied concentrations of alpha-actinin to introduce a load to the assay. We found that E525K required significantly more alpha-actinin to slow the in vitro gliding velocities 50% (EC50 = $16.2 \pm 1.0$ and $10.6 \pm 1.1$ ug/mL for E525K and WT, respectively) when the data in Figure 5B were fit to a standard dose–response curve. We utilized the assumptions from Greenberg and
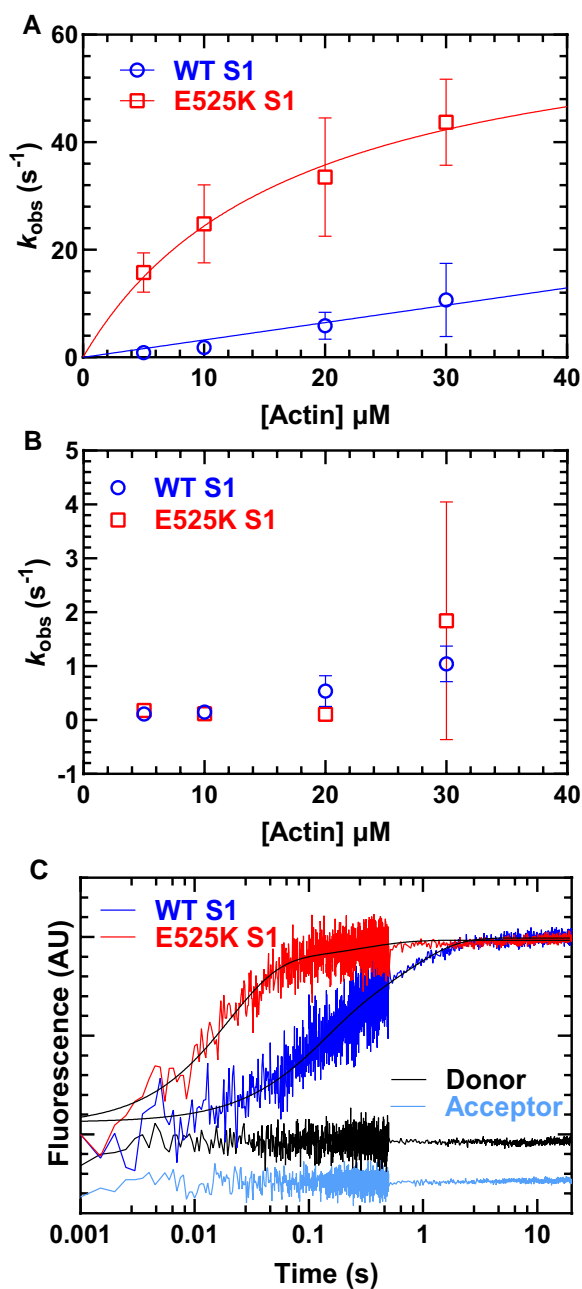
**Fig. 4.** Actin-activated power stroke. Actin-activated power stroke rate constants were measured by monitoring the fluorescence enhancement of Alexa 488 RLC (FRET) during actin-activated product release. Sequential-mix stopped-flow experiments were performed by mixing M2β S1 A488RLC Cy3ATP, aged for 10 s for hydrolysis to occur, and then mixed with actin (final concentrations: 0.5 μM M2B S1, 0.45 μM ATP, and 5–30 μM actin). The fluorescence transients were best fit by a double exponential function. A) The rate constants of the fast phase were plotted as a function of actin concentration and fitted to a hyperbolic function for E525K and WT. B) The slow phase of the power stroke was relatively independent of actin concentration. C) Representative fluorescence transients in the presence of 30 μM actin (average of two transients) are shown fitted to a double exponential function. The donor-only and acceptor-only controls are shown for comparison. Data points at each actin concentration represent the average ± SD of three experiments from separate protein preparations. Some error bars are not visible because they are smaller than the symbols.

Moore to convert alpha-actinin concentration to viscous load, which allowed us to fit the data to the force–velocity relationship (30). We determined that the mutant generated a larger (2.6-fold)

maximum ensemble force (or isometric force). We also plotted the force as a function of power and found that E525K generated a 4.6-fold higher peak power and the force at which peak power was observed was also increased (threefold). Our results strongly complement our kinetic characterization and clearly demonstrate that this mutation enhances both enzymatic and motor properties.

## Atomistic simulations reveal mechanistic differences between WT and E525K actomyosin

To investigate the impact of the E525K mutant on the myosin power stroke at an atomistic level, we carried out Gaussian accelerated MD (GaMD) simulations on the prepower stroke (PPS) actomyosin structure (Fig. 6A) (31). The E525K simulations were set up based on models obtained for the WT PPS actomyosin complex (32). We found that the N-terminus of actin can form an interaction directly with the activation loop (E525K) (Fig. 6B). In contrast, in the WT simulations, E525 was unable to form interactions with the negatively charged residues at the actin N-terminus. Our analysis shows that the WT PPS myosin can form a salt bridge between E525 and K484, which has a most probable distance of 3.5Å (cyan curve in Fig. 6D). In the case of E525K simulations, this salt bridge is destabilized and the most probable K525-K484 distance increases to 6.5 Å (orange curve in Fig. 6D), accompanied by rotations of the relay helix (RH, Fig. 6C). The E525K mutant displays more pronounced variations in the relay helix (RH) motion compared to the WT case, as shown in Fig. S7. These changes further induce a metastable state of the active site, characterized by a widened gap between switch I and II (Fig. 6E). The free energy profile along the distance between switch I and switch II finds this metastable state (17Å) to be exclusive to the E525K simulations (highlighted by the black dotted line in Fig. 6F). Given that switch I and II are proposed to form the "back door" for phosphate release, the widening of the gate represents an intermediate state potentially facilitating phosphate release. Our results suggest an allosteric mechanism that is adopted by the E525K mutant to promote Pi release and power stroke transition (further discussed below).

## Discussion

We completed a comprehensive analysis of the E525K mutation in monomeric M2β S1, which allowed us to determine the impact of the mutation on the ATPase mechanism, duty ratio, motile properties, and structural mechanism of force generation. We revealed that the threefold increase in steady-state actin-activated ATPase activity is explained primarily by significantly enhanced actin-activated power stroke and phosphate release rate constants. With only minor changes to the other steps in the ATPase cycle, the enhancement in the power stroke/phosphate release increases the duty ratio approximately threefold in the E525K mutation. Our in vitro motility results align with the kinetic characterization by demonstrating increases in actin gliding velocity, ensemble force, and power. We also performed Gaussian molecular dynamics simulations, which allowed us to propose a specific allosteric pathway for actin activation of the power stroke and phosphate release. Lysine 484 in the relay helix forms an essential salt bridge with glutamate 525 in the activation loop that is abolished by the mutation. The resulting increased flexibility of the relay helix and activation loop facilitates the enhanced actin activation mechanism. In a previous study, we demonstrated that the E525K mutation dramatically stabilizes the autoinhibited
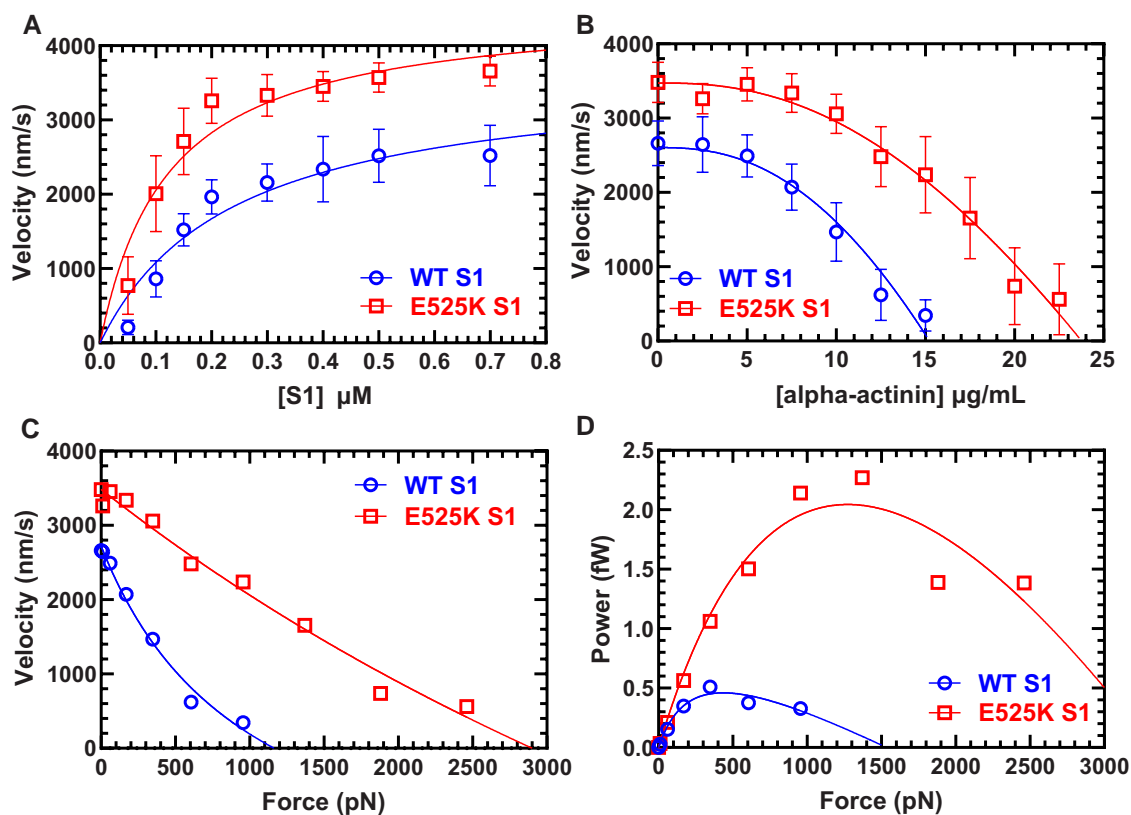
**Fig. 5.** Actin gliding, ensemble force, and power. A) Actin sliding velocities were quantified across a range of myosin surface densities in an in vitro motility assay. Surface density modulation was achieved by varying myosin incubation concentrations within the range of 0.05–0.7 μM. Data points were presented as the mean ± SD, with measurements conducted using three separate protein preparations. A total of 150 actin filaments (50 actin filaments per protein preparation, $N = 3$) were assessed for each condition. B) To investigate the impact of frictional load, alpha-actinin, an actin binding protein was employed. The total concentration of M2β S1 loaded onto the surface remained constant at 0.4 μM, while the concentration of alpha-actinin was varied within the range of 0–22.5 μg/mL until a point of actin filament movement cessation was reached. A total of 100 actin filaments from three distinct protein preparations were examined. Data were fitted to the elastic model (30). The error bars presented are the mean ± SD. C) Using the data from Fig. 5B, alpha-actin concentrations were converted to viscous load, which allowed us to fit the data to the force–velocity relationship. The data were fit to the Hill equation as described by Greenberg and Moore (30), resulting in the determination of the maximum ensemble force ($F_{MAX}$). D) Data from force–velocity relationship (Fig. 5C) were transformed into power by multiplying the force by the velocity, subsequently facilitating the generation of power-force plots. Peak power values and the corresponding force at which peak power occurred were determined by plotting and fitting the curve to the Hill equation. These results are summarized in Table 3.

**Table 3.** Summary of in vitro motility measurements.

| Motor Property | WT S1 | E525K S1 |
|---|---|---|
| Maximum unloaded sliding velocity ($V_{MAX}$) (nm$^{-1}$s$^{-1}$) | 3663 ± 63 | *4535 ± 44 |
| Density at which unloaded V is ½ $V_{MAX}$ (μM) ($K_{0.5}$) | 0.239 ± 0.010 | *0.121 ± 0.004 |
| EC50 for alpha-actinin (μg/mL) | 10.6 ± 1.1 | *16.2 ± 1.0 |
| Maximum ensemble force ($F_{MAX}$) (pN) | 796 ± 51 | *2040 ± 79 |
| Peak power (fW) | 0.45 | 2.05 |
| Force at which peak power occurs (pN) | 425 | 1273 |

*$P < 0.05$. Errors reported are standard error of the fit ($N = 3$).

state in dimeric heavy meromyosin (HMM) (10). Therefore, we propose that an important feature of the autoinhibited state is its ability to sequester the lower 50 kDa domain region containing the activation loop from interacting with actin, subsequently preventing initiation of the highly conserved actin activation pathway. In addition, this study sheds light on the balance between intrinsic motor properties and autoinhibition, and the interplay between these factors that ultimately leads to the reduced force and power observed in DCM patients.

## Impact of DCM mutant E525K on intrinsic ATPase cycle kinetics

Steady-state ATPase measurements uncovered that the E525K mutation increased the actin-activated ATPase approximately threefold and dramatically reduced (eightfold) the actin concentration required to reach one-half maximal ATPase. Impressively, the catalytic efficiency ($k_{cat}/K_{ATPase}$) was improved 20-fold in the mutant. We did observe a twofold increase in ATPase activity in the absence of actin, demonstrating the mutation alters the rate-limiting step, likely phosphate release, in the absence of actin. The current study differs from our previous work, in that we used a buffer with lower ionic strength and a higher magnesium concentration (MOPS 5/4). Transient kinetic analysis revealed the mutation only resulted in minor changes to ATP binding, hydrolysis, and ATP-induced dissociation from actin, with no significant changes or minor changes in ADP release. Actin-activated phosphate release experiments, measured using the phosphate-binding protein, revealed a twofold increase in the fast phase of the fluorescence transients, similar to that observed with steady-state ATPase. However, the slow phase was quite similar in both mutant and WT. In general, our phosphate release results agree with what has been previously reported in the literature for WT M2β S1. *Tang* et al. (25) reported two phases in the
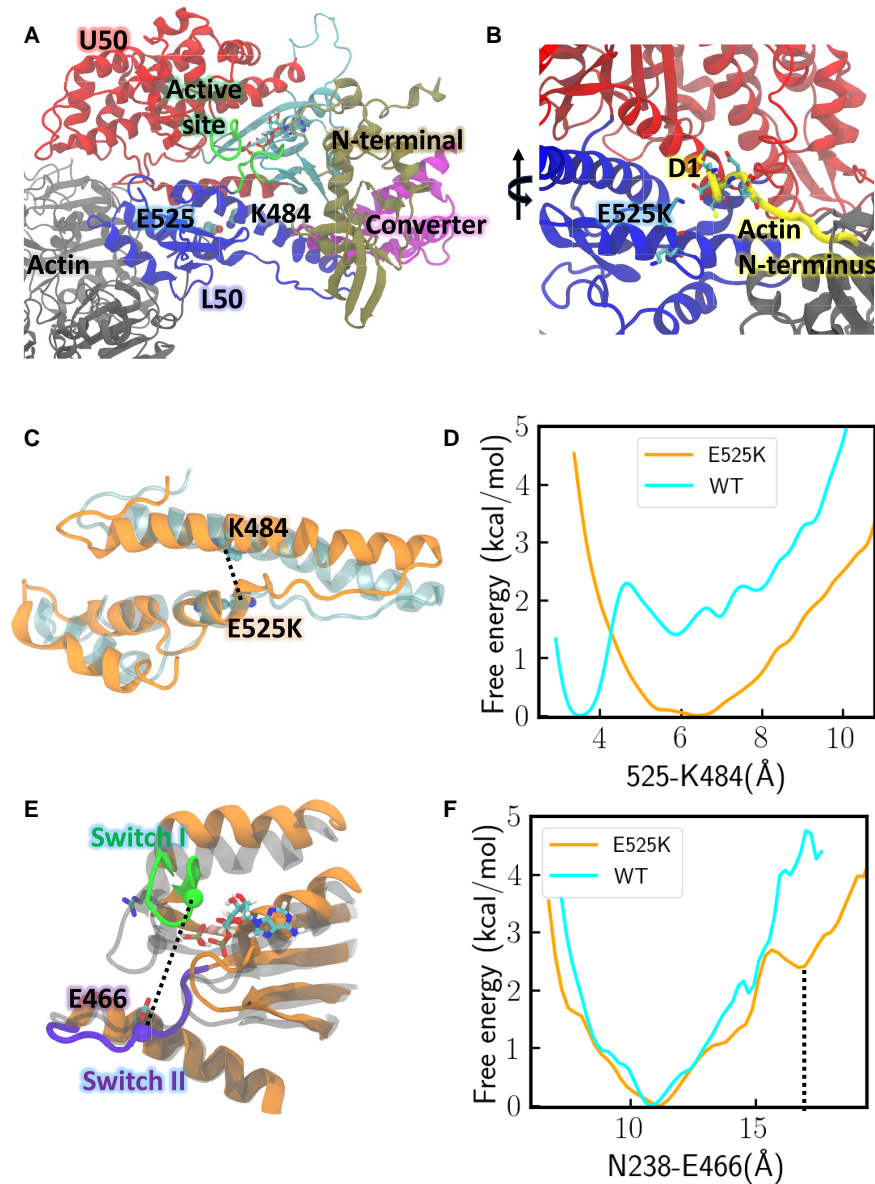
**Fig. 6.** GaMD simulations reveal differences between WT and E525K myosin. A) A structural model for the prepower stroke (PPS) actomyosin with domains, $Mg^{2+}$, ADP, and Pi shown. B) In the mutant E525K simulations, a metastable salt bridge was observed between E525K and D1 (the N-terminus of actin). C) Representative conformations of the relay helix and helix loop helix (HLH) motif for the E525K actomyosin simulations (orange) and WT actomyosin simulations (cyan) at the PPS state. D) The free energy profiles projected along the distance between residues 525 and K484. E) For the E525K mutant, myosin active site in the presence of $Mg^{2+}$, ADP, and Pi at the most probable state is shown in transparent gray, whereas the active site at a metastable state is shown in orange (switch I in green, switch II in purple). F) The free energy profiles projected along the distance between N238 (switch I) and E466 (switch II). The metastable state shown in panel D is highlighted by the black dotted line. This state, which is only observed in the E525K simulations (orange curve), likely facilitates Pi release.

phosphate release transients at 30 μM actin with similar slow and fast phase rate constants. However, another study from our group (24) revealed transients with a subtle lag followed by a single exponential phase that was equivalent to the slow phase in our current study and the previous *Tang* et al. *2019* study (25). Thus, M2β S1 phosphate release transients are dominated by a slow component and a minor fast component that can be difficult to detect since its relative amplitude is quite small (10–20%). Two other studies performed phosphate release with recombinant M2β HMM and regulated thin filaments and found fluorescence transients with fast and slow components with similar rate constants to our work, while the fast component contained a larger relative amplitude (28, 33).

The actin-activated power stroke was measured using a FRET approach that detects the rotation of the lever arm during the transition between the pre and post-power stroke states. Transients were best fit to a double exponential function, with similar rate constants for WT M2β S1 as were found in our previous study (24). FRET experiments demonstrated the mutation enhanced the fast power stroke rate constant fourfold. Overall, the fast phase of the power stroke and phosphate release were similar in both the mutant and WT constructs, suggesting the two steps may be indistinguishable in cardiac myosin. This is in contrast to our studies on myosin V that demonstrated the power stroke occurs faster than phosphate release and provided direct evidence that the power stroke precedes the slower phosphate

release step (34). The duty ratio, which can be calculated by performing simulations using the proposed kinetic model (Table S1), was found to be increased threefold in the mutant.

It is tempting to speculate that the slow phase in the power stroke and phosphate release transients is derived from the actin-bound hydrolysis step. Previous work from White and colleagues has provided strong evidence that this pathway exists in the fast skeletal muscle myosin ATPase mechanism and later in porcine cardiac myosin (28, 35). Our data is best fit to a scheme that includes two pathways, an actin-bound ATP hydrolysis pathway and the canonical pathway with ATP hydrolysis off actin following by tightly coupled power stroke and phosphate release (see Table S1 and Fig. S6F) (35–37). Other pathways cannot currently be ruled out, such as a slow and fast pathway for phosphate release, and thus further studies may be necessary to define the rate-limiting steps in the cardiac muscle myosin ATPase cycle. We found the relative amplitude of the fast component of the power stroke transients were greater than the fast component of phosphate release transients in both WT and E525K. We speculate that the lever arm rotation may be altered (e.g. reducing the amplitude of the FRET signal) in the actin-bound hydrolysis pathway, while the canonical pathway provides a greater FRET amplitude associated with the actin-activated power stroke.

## E525K enhances actin gliding, ensemble force, and power

By characterizing the motile properties of the E525K mutant, we found that the enhanced duty ratio observed in our kinetic studies translates to increased ensemble force and power. Several other studies have compared duty ratio and ensemble force and power using the alpha-actinin loaded motility assay (30, 38–40). Our results demonstrate that E525K does not disrupt the mechanism of force production, which is thought to be rotation of the lever arm while myosin is tightly bound to actin. Thus, our motility results reinforce our measurements of the power stroke rate constant, which found that lever arm rotation was accelerated by the mutation and suggest the mutation does not impair the conserved structural mechanism of force generation but simply accelerates key aspects of the mechanism. The more rapid transition into the strongly bound state with little change in the transition into the weakly bound intermediates will allow more force generating motors to interact with actin filaments at any given time and increase the ensemble force of the mutant compared to WT. Alternatively, individual E525K mutant motors may have a greater force generating capacity. This could be accomplished by changing the mechanical properties of the lever arm, which was observed in other studies (41, 42). Thus, it will be important to examine the single molecule mechanical properties of the E525K mutation to further investigate the mechanism of how it enhances ensemble force and power.

The increase in velocity observed with the mutant was unexpected since the ADP release rate constant, which typically correlates with unloaded sliding velocity, was unchanged or only slightly changed (43). We found a 12% change in the mant-ADP release rate constant and no change in ADP release from pyrene actomyosin. Classic models of muscle contraction predict that the ADP release rate constant should control the detachment rate which suggests detachment limited sliding velocity (44). It is well established that the ADP release rate constant can be altered by free $Mg^{2+}$ (26). Thus, we performed mant-ADP release experiments with a range of $MgCl_2$ concentrations and found that at low $MgCl_2$ (1 mM) the ADP release rate constant with E525K was twofold faster than what we measured at 4 mM $MgCl_2$, while

WT displayed only a 12% increase (Fig. S6 and Table S2). This indicates that the $Mg^{2+}$ affinity for E525K in the presence of ADP may be significantly reduced. In our GaMD simulations, we did not observed any difference in the $Mg^{2+}$ coordination in the pre-power stroke actomyosin structure of the E525K mutant. However, simulations in the actomyosin ADP state will be an excellent avenue for future studies. Since we utilized a lower $MgCl_2$ concentration for our motility assay, which we found to be more amenable for performing the loaded assay, we also assessed unloaded sliding velocity in the higher $MgCl_2$ (4 mM) buffer but still found the E525K was faster than WT. Thus, the enhanced sliding velocity of E525K cannot be explained by changes in the ADP release rate constant. Early studies by Barany found a correlation between ATPase rate, which is thought to be attachment limited in muscle myosins, and muscle shortening velocity (44). Recent studies by the Baker and Cremo groups have developed a model that suggests maximum velocity is dependent on both attachment (40%) and detachment (60%) kinetics (45). Thus, the E525K mutation which accelerates ATPase and attachment kinetics, but causes little change in detachment kinetics, seems to provide further evidence for attachment-limited models of in vitro actin gliding. In another study performed in parallel with this work, we found that dimeric beta-cardiac myosin constructs containing the E525K mutation did not alter the unloaded in vitro gliding velocity compared to WT counterparts (46). We hypothesize that the impact of E525K on attachment kinetics may be diminished with dimeric constructs, which is consistent with the idea that dimeric myosin cooperatively binds to actin (47). Alternatively, the strategy for adhering myosin to the motility surface was different in Duno-Miranda study (anti-GFP nanobody) compared to the current study (anti-GFP antibody) (46).

## Allosteric mechanism of actin activation

Our work has uncovered key structural details of the allosteric pathway associated with actin activation of the ATPase cycle. The activation loop, located in the lower 50 kDa domain of the actin binding region, is a highly conserved loop across myosin isoforms that was first discovered in *Dictyostelium* myosin (21). The loop was termed "activation loop" for its ability to influence actin activation kinetics in *Dictyostelium* myosin without introducing any other significant changes to the ATPase mechanism in the absence of actin (21). This loop varies in size depending on the specific isoform, ranging from about 5 to 10 residues in length. Each activation loop across the myosin family contains a positively charged amino acid at the tip, such as arginine 520 in *Dictyostelium* myosin and lysine 526 in cardiac myosin (see Fig. S1 for alignment). This positive charge is thought to be essential for interactions with the N-terminus of actin, which promotes the rotation of the lower 50 kDa domain during the transition from pre to post-power stroke states and the release of phosphate (22).

The conserved intrinsic structural transitions during myosin force generation are still being elucidated. Actin-bound myosin, with the products of ATP hydrolysis in the active site, undergoes key conformational changes that require allosteric communication between the active site and the actin binding region as well as the converter/lever arm. The changes in the active site promote the release of phosphate, while the changes in the converter/lever arm promote rotation of the lever arm into the post-power stroke state. During this process, ADP remains in the active site, while phosphate has been proposed to exit though a "back door" mechanism gated by an essential salt bridge between switch I and switch II (48, 49). In cardiac myosin, glutamate 525 at the base

of the activation loop forms a salt bridge with lysine 484 of the relay helix. Substituting lysine at the 525 position disrupts this salt bridge making the relay helix more flexible. Increased flexibility of the relay helix induces a metastable state in which the gap between switch I and switch II that gates phosphate release is widened. This "open door" allows phosphate to exit expeditiously. The converter domain, at the opposite end of the relay helix, is also altered by the increased relay helix flexibility. Simulations show that the region containing the relay helix, activation loop, and helix-loop-helix motif, in the E525K construct shifts towards a more rigor-like conformation that could explain the observed power stroke acceleration. Positioned adjacent to the activation loop, the helix-loop-helix motif is proposed to form stable interactions with actin during the early stages of actin binding (32). In addition, disruption of the salt bridge interaction between the relay helix and activation loop allows the loop (E525K) to interact with the negatively charged N-terminus of actin (e.g. D1) (Fig. 6B), further facilitating the actin activation mechanism in the mutant. The interaction of E525K with actin provides a structural basis for the enhanced actin affinity (reduced $K_{ATPase}$) observed with this mutant (Fig. 2). Steady-state ATPase activity is increased twofold in the E525K mutant in the absence of actin, which may result from enhanced relay helix flexibility. Overall, in the absence of the critical salt bridge, actin binding may cause the relay helix to more rapidly transition into conformations that promote the open back door and post-power stroke lever arm.

## Impact of E525K on IHM formation

A detailed mechanism for how the autoinhibited IHM prevents interaction with actin and thus force generation is currently unclear. Generally, it is understood that the heads of the motor domain fold back asymmetrically onto the S2 rod as well as interact with each other inhibiting interactions with actin. Our previous work relied on a tarantula myosin homology model (PDB 5TBY) to predict the role of E525K on IHM structural interactions (10, 50). Recently, an updated 3.6 Å cryoEM model of the human beta-cardiac myosin IHM (PDB 8ACT) has become available (51). The region containing the E525K mutation, the activation loop, and the portion of the lower 50 kDa domain proposed to be involved in the conserved actin activation mechanism are sequestered in the IHM in both models. A model of the IHM based on the 8ACT structure reveals that D900 and E903 in the S2 region are in close proximity to E525 in the blocked head (BH) (Fig. S8). Thus, the E525K mutation may stabilize the IHM by forming a salt bridge with D900 or E903. Overall, we propose that a principal feature of the autoinhibition mechanism of the IHM conformation is that it prevents this region of the myosin motor domain from interacting with actin, subsequently hindering the actin activation mechanism. It is interesting to speculate on how this hypothesis will be realized in a muscle fiber where the activation loop region of myosin can either bind to actin to produce force or interact with S2 to form the IHM. Since we propose that E525K has enhanced affinity for both actin and S2, we suggest there will be less myosin heads interacting with actin but those able to interact will be capable of enhanced force and power.

## Implications for understanding underlying mechanisms of DCM

Dilated cardiomyopathy *MYH7* mutations are thought to decrease intrinsic motor properties and/or stabilize the autoinhibited state leading to reduced force and power (10, 25, 50, 52). In contrast, HCM mutations are thought to increase intrinsic motor properties and/or destabilize the autoinhibited state leading to increased force and power (23, 53, 54). Interestingly, in some cases HCM mutations trigger a decrease in intrinsic motor properties while also causing destabilization of the autoinhibited state (19, 20, 55, 56). Thus, it is crucial to understand the interplay between these two factors to elucidate genotype-phenotype relationships. The E525K mutant is cited in ClinVar primarily as a DCM implicated mutation with one incidence of HCM and left ventricular noncompaction (LVNC) reported. However, these reports of E525K resulting in additional myopathic pathogeneses still acknowledge E525K as a clinically significant DCM mutant (57). The E525K mutant is an intriguing example of a DCM mutant that can stabilize the autoinhibited state while also increasing the intrinsic motor properties of active heads. Ensemble force can be represented as the product of the number of available heads, the duty ratio, and the intrinsic force of each myosin head (18). Because E525K mutants present as DCM, it is attractive to hypothesize that the ability of E525K to stabilize the autoinhibited state dominates the increases observed in intrinsic motor properties. It is also important to note that the complexity of the mechanism's opposing parameters could explain the sparse incidence of HCM and LVNC. Although uncommon, unbalanced myocardial performance early in life could present as one form of cardiomyopathy (e.g. LVNC or HCM) before later evolving into DCM (58, 59).

In addition, DCM is known to present with reduced Frank–Starling response, where cardiac muscle has enhanced force generation upon stretch, which makes the tissue less efficient at keeping up with systemic demand (60–65). When muscle is stretched in the presence of load, myosin heads are proposed to be released from the SRX/IHM states (65). This shift allows heads to move away from the thick filament backbone and become readily available to form cross bridges (65). E525K could impair Frank–Starling mediated force increases due to stabilization of the SRX/IHM states, preventing stretch-activation of the thick filament. Because E525K may primarily cause DCM by stabilizing the autoinhibited state, the first inclination would be to treat with an IHM destabilizing therapeutic. However, it is important to note this may trigger the enhanced actin activation mechanism that is concealed by the IHM conformation. Mobilization of the previously sequestered but more powerful motors may lead patients to display hypercontractility and relaxation defects. Further study of the intricately balanced myosin force generating system will continue to elucidate DCM pathogenesis and drive therapeutic development.

## Limitations and future directions

It is important to acknowledge any limitations and possible alternative interpretations in the current study. The WT and E525K M2β S1 constructs were examined with endogenous mouse light chains intrinsic to the C2C12 myocyte expression system. This could potentially alter the impact of the E525K mutation, though the location of the mutation makes this unlikely in an S1 construct. In the current study, we were not able to assess the force generating properties of E525K in a simulated thick filament environment. Future studies will perform mechanical measurements with synthetic thick filaments generated with a DNA origami platform (66). Also, utilizing a human induced pluripotent stem cell cardiomyocyte (hiPSC-CM) model would allow for examining the influence of regulatory proteins such as cardiac myosin binding protein C.

## Conclusions

In summary, this study revealed an important allosteric pathway associated with actin activation of the myosin power stroke and

product release, which we propose is crucial for the actomyosin ATPase mechanism. We suspect that this is a highly conserved allosteric pathway since the critical salt bridge we identified is conserved throughout most of the myosin superfamily. Our detailed characterization of the E525K mutation in the activation loop also suggests sequestering this element of the actin binding region in the folded-back autoinhibited IHM is crucial for preventing actin activation of the ATP hydrolysis cycle and force generation. Our work further demonstrates the complexity of cardiomyopathy-associated mutations in beta-cardiac myosin, since E525K significantly increases duty ratio, ensemble force and power in monomeric subfragment 1 while stabilizing the SRX state and IHM conformation. Thus, there is a delicate balance between intrinsic motor properties of myosin heads recruited to bind the actin thin filament and the ability to autoinhibit myosin heads in the thick filament, which ultimately controls force generation in cardiac muscle. The severity of the cardiomyopathy phenotype, whether it be the enhanced contractile force and disrupted relaxation observed in HCM or the depressed force observed in DCM, will depend on the interplay between these two key factors. Thus, detailed biophysical characterization of cardiomyopathy-associated mutations in sarcomeric proteins will help guide future therapies that attempt to normalize these key factors that are crucial for controlling cardiac contractility.

## Materials and methods

Detailed materials and methods are outlined in supplemental Appendix, *Materials and Methods*.

## Acknowledgments

## Preprint

This manuscript was posted as a preprint: https://doi.org/10.1101/2023.11.10.566646.

## Supplementary Material

Supplementary material is available at *PNAS Nexus* online.

## Funding

## Author Contributions

S.M.L.B. and C.M.Y. developed the rationale for the project and performed all kinetics experiments. J.G. performed unloaded and loaded in vitro motility assays. W.M. and J.A.M. contributed gaussian accelerated molecular dynamics simulations and analysis. D.V.R. and R.D. provided support in molecular cloning, virus amplification, and cell culture. S.M.L.B., C.M.Y., J.G., and W.M. wrote the original draft. The manuscript was reviewed and approved by all authors.

## Data Availability

All of the data described in this study are included in the manuscript and/or supplemental information.

## References

1  Geeves MA. 2016. Review: the ATPase mechanism of myosin and actomyosin. *Biopolymers*. 105:483–491.

2  Sellers JR. 2000. Myosins: a diverse superfamily. *Biochim Biophys Acta (BBA)—Mol Cell Res*. 1496:3–22.

3  Gordon AM, Homsher E, Regnier M. 2000. Regulation of contraction in striated muscle. *Physiol Rev*. 80:853–924.

4  Huxley AF. 1957. Muscle structure and theories of contraction. *Prog Biophys Biophys Chem*. 7:255–318.

5  Nag S, Trivedi DV. 2021. To lie or not to lie: super-relaxing with myosins. *Elife*. 10:e63703.

6  Stewart MA, Franks-Skiba K, Chen S, Cooke R. 2010. Myosin ATP turnover rate is a mechanism involved in thermogenesis in resting skeletal muscle fibers. *Proc Natl Acad Sci U S A*. 107:430–435.

7  Anderson RL, *et al.* 2018. Deciphering the super relaxed state of human beta-cardiac myosin and the mode of action of mavacamten from myosin molecules to muscle fibers. *Proc Natl Acad Sci U S A*. 115:E8143–E8152.

8  McNamara JW, Li A, Dos Remedios CG, Cooke R. 2015. The role of super-relaxed myosin in skeletal and cardiac muscle. *Biophys Rev*. 7:5–14.

9  Hooijman P, Stewart MA, Cooke R. 2011. A new state of cardiac myosin with very slow ATP turnover: a potential cardioprotective mechanism in the heart. *Biophys J*. 100:1969–1976.

10  Rasicci DV, *et al.* 2022. Dilated cardiomyopathy mutation E525K in human beta-cardiac myosin stabilizes the interacting-heads motif and super-relaxed state of myosin. *Elife*. 11:e77415.

11  Preller M, Manstein DJ. 2013. Myosin structure, allostery, and mechano-chemistry. *Structure*. 21:1911–1922.

12  Yotti R, Seidman CE, Seidman JG. 2019. Advances in the genetic basis and pathogenesis of sarcomere cardiomyopathies. *Annu Rev Genomics Hum Genet*. 20:129–153.

13  Keam SJ. 2022. Mavacamten: first approval. *Drugs*. 82:1127–1135.

14  Chuang C, *et al.* 2021. Discovery of aficamten (CK-274), a next-generation cardiac myosin inhibitor for the treatment of hypertrophic cardiomyopathy. *J Med Chem*. 64:14142–14152.

15  Morgan BP, *et al.* 2010. Discovery of omecamtiv mecarbil the first, selective, small molecule activator of cardiac myosin. *ACS Med Chem Lett*. 1:472–477.

16  Voors AA, *et al.* 2020. Effects of danicamtiv, a novel cardiac myosin activator, in heart failure with reduced ejection fraction: experimental data and clinical results from a phase 2a trial. *Eur J Heart Fail*. 22:1649–1658.

17  Woody MS, *et al.* 2018. Positive cardiac inotrope omecamtiv mecarbil activates muscle despite suppressing the myosin working stroke. *Nat Commun*. 9:3838.

18  Spudich JA. 2014. Hypertrophic and dilated cardiomyopathy: four decades of basic research on muscle lead to potential therapeutic approaches to these devastating genetic diseases. *Biophys J*. 106:1236–1249.

19  Morck MM, *et al.* 2022. Hypertrophic cardiomyopathy mutations in the pliant and light chain-binding regions of the lever arm of human beta-cardiac myosin have divergent effects on myosin function. *Elife*. 11:e76805.

20  Bell KM, Kronert WA, Huang A, Bernstein SI, Swank DM. 2019. The R249Q hypertrophic cardiomyopathy myosin mutation

decreases contractility in Drosophila by impeding force production. *J Physiol.* 597:2403–2420.

21 Várkuti BH, *et al.* 2012. A novel actin binding site of myosin required for effective muscle contraction. *Nat Struct Mol Biol.* 19: 299–306.

22 Llinas P, *et al.* 2015. How actin initiates the motor activity of myosin. *Dev Cell.* 33:401–412.

23 Spudich JA. 2015. The myosin mesa and a possible unifying hypothesis for the molecular basis of human hypertrophic cardiomyopathy. *Biochem Soc Trans.* 43:64–72.

24 Tang W, Ge J, Unrath WC, Desetty R, Yengo CM. 2021. Cardiomyopathy mutations impact the actin-activated power stroke of human cardiac myosin. *Biophys J.* 120:2222–2236.

25 Tang W, Unrath WC, Desetty R, Yengo CM. 2019. Dilated cardiomyopathy mutation in the converter domain of human cardiac myosin alters motor activity and response to omecamtiv mecarbil. *J Biol Chem.* 294:17314–17325.

26 Swenson AM, *et al.* 2014. Magnesium modulates actin binding and ADP release in myosin motors. *J Biol Chem.* 289:23977–23991.

27 De La Cruz EM, Ostap EM. 2009. Kinetic and equilibrium analysis of the myosin ATPase. *Methods Enzymol.* 455:157–192.

28 Liu Y, White HD, Belknap B, Winkelmann DA, Forgacs E. 2015. Omecamtiv mecarbil modulates the kinetic and motile properties of porcine β-cardiac myosin. *Biochemistry.* 54:1963–1975.

29 Deacon JC, Bloemink MJ, Rezavandi H, Geeves MA, Leinwand LA. 2012. Identification of functional differences between recombinant human α and β cardiac myosin motors. *Cell Mol Life Sci.* 69: 2261–2277.

30 Greenberg MJ, Moore JR. 2010. The molecular basis of frictional loads in the in vitro motility assay with applications to the study of the loaded mechanochemistry of molecular motors. *Cytoskeleton.* 67:273–285.

31 Miao Y, Feher VA, McCammon JA. 2015. Gaussian accelerated molecular dynamics: unconstrained enhanced sampling and free energy calculation. *J Chem Theory Comput.* 11:3584–3595.

32 Ma W, You S, Regnier M, McCammon JA. 2023. Integrating comparative modeling and accelerated simulations reveals conformational and energetic basis of actomyosin force generation. *Proc Natl Acad Sci U S A.* 120:e2215836120.

33 Snoberger A, *et al.* 2021. Myosin with hypertrophic cardiac mutation R712L has a decreased working stroke which is rescued by omecamtiv mecarbil. *Elife.* 10:e63691.

34 Gunther LK, *et al.* 2020. FRET and optical trapping reveal mechanisms of actin activation of the power stroke and phosphate release in myosin V. *J Biol Chem.* 295:17383–17397.

35 White HD, Belknap B, Webb MR. 1997. Kinetics of nucleoside triphosphate cleavage and phosphate release steps by associated rabbit skeletal actomyosin, measured using a novel fluorescent probe for phosphate. *Biochemistry.* 36:11828–11836.

36 Stein LA, Schwarz RP Jr, Chock PB, Eisenberg E. 1979. Mechanism of the actomyosin adenosine triphosphatase. Evidence that adenosine 5'-triphosphate hydrolysis can occur without dissociation of the actomyosin complex. *Biochemistry.* 18:3895–3909.

37 Stein LA, White MP. 1987. Biochemical kinetics of porcine cardiac subfragment-1. *Circ Res.* 60:39–49.

38 Bing W, Knott A, Marston SB. 2000. A simple method for measuring the relative force exerted by myosin on actin filaments in the in vitro motility assay: evidence that tropomyosin and troponin increase force in single thin filaments. *Biochem J.* 350 Pt 3:693–699.

39 Haeberle JR. 1994. Calponin decreases the rate of cross-bridge cycling and increases maximum force production by smooth muscle myosin in an in vitro motility assay. *J Biol Chem.* 269: 12424–12431.

40 Janson LW, Sellers JR, Taylor DL. 1992. Actin-binding proteins regulate the work performed by myosin II motors on single actin filaments. *Cell Motil Cytoskeleton.* 22:274–280.

41 Kad NM, Patlak JB, Fagnant PM, Trybus KM, Warshaw DM. 2007. Mutation of a conserved glycine in the SH1-SH2 helix affects the load-dependent kinetics of myosin. *Biophys J.* 92:1623–1631.

42 Batra R, Geeves MA, Manstein DJ. 1999. Kinetic analysis of Dictyostelium discoideum myosin motor domains with glycine-to-alanine mutations in the reactive thiol region. *Biochemistry.* 38:6126–6134.

43 Siemankowski RF, Wiseman MO, White HD. 1985. ADP dissociation from actomyosin subfragment 1 is sufficiently slow to limit the unloaded shortening velocity in vertebrate muscle. *Proc Natl Acad Sci U S A.* 82:658–662.

44 Bárány M. 1967. ATPase activity of myosin correlated with speed of muscle shortening. *J Gen Physiol.* 50:197–218.

45 Stewart TJ, Murthy V, Dugan SP, Baker JE. 2021. Velocity of myosin-based actin sliding depends on attachment and detachment kinetics and reaches a maximum when myosin-binding sites on actin saturate. *J Biol Chem.* 297:101178.

46 Duno-Miranda S, *et al.* 2024. Tail length and E525K dilated cardiomyopathy mutant alter human β-cardiac myosin super relaxed state. *J Gen Physiol.* 156:e202313522.

47 Conibear PB, Geeves MA. 1998. Cooperativity between the two heads of rabbit skeletal muscle heavy meromyosin in binding to actin. *Biophys J.* 75:926–937.

48 Holmes KC, Geeves MA. 2000. The structural basis of muscle contraction. *Philos Trans R Soc Lond. Ser B: Biol Sci.* 355:419–431.

49 Yount RG, Lawson D, Rayment I. 1995. Is myosin a "back door" enzyme? *Biophys J.* 68:44S–47S; discussion 47S-49S.

50 Alamo L, *et al.* 2017. Effects of myosin variants on interacting-heads motif explain distinct hypertrophic and dilated cardiomyopathy phenotypes. *Elife.* 6:e24634.

51 Grinzato A, *et al.* 2023. Cryo-EM structure of the folded-back state of human β-cardiac myosin. *Nat Commun.* 14:3166.

52 Ujfalusi Z, *et al.* 2018. Dilated cardiomyopathy myosin mutants have reduced force-generating capacity. *J Biol Chem.* 293: 9017–9029.

53 Trivedi DV, Adhikari AS, Sarkar SS, Ruppel KM, Spudich JA. 2018. Hypertrophic cardiomyopathy and the myosin mesa: viewing an old disease in a new light. *Biophys Rev.* 10:27–48.

54 Robert-Paganin J, Auguin D, Houdusse A. 2018. Hypertrophic cardiomyopathy disease results from disparate impairments of cardiac myosin function and auto-inhibition. *Nat Commun.* 9:4019.

55 Nandwani N, *et al.* Hypertrophic cardiomyopathy mutations Y115H and E497D disrupt the folded-back state of human beta-cardiac myosin allosterically. bioRxiv 582851. https://doi.org/10.1101/2024.02.23.582851, 3 March 2024, preprint: not peer reviewed.

56 Kawana M, Sarkar SS, Sutton S, Ruppel KM, Spudich JA. 2017. Biophysical properties of human β-cardiac myosin with converter mutations that cause hypertrophic cardiomyopathy. *Sci Adv.* 3:e1601959.

57 Lakdawala NK, *et al.* 2012. Genetic testing for dilated cardiomyopathy in clinical practice. *J Card Fail.* 18:296–303.

58 Spillmann F, *et al.* 2016. Reversible transition from a hypertrophic to a dilated cardiomyopathy. *ESC Heart Fail.* 3:138–142.

59 Kawana A, Imaoka C, Kanemoto N. 1987. Evolution of dilated cardiomyopathy from hypertrophic obstructive cardiomyopathy: a case report. *J Cardiol.* 17:389–398.

60 Zhang X, *et al.* 2017. Distinct contributions of the thin and thick filaments to length-dependent activation in heart muscle. *Elife.* 6:e24081.

61 Reconditi M, *et al.* 2017. Myosin filament activation in the heart is tuned to the mechanical task. *Proc Natl Acad Sci U S A*. 114:3240–3245.

62 Brunello E, *et al.* 2020. Myosin filament-based regulation of the dynamics of contraction in heart muscle. *Proc Natl Acad Sci U S A*. 117:8177–8186.

63 Ait-Mou Y, *et al.* 2016. Titin strain contributes to the Frank-Starling law of the heart by structural rearrangements of both thin- and thick-filament proteins. *Proc Natl Acad Sci U S A*. 113:2306–2311.

64 Caremani M, *et al.* 2019. Inotropic interventions do not change the resting state of myosin motors during cardiac diastole. *J Gen Physiol*. 151:53–65.

65 Ma W, *et al.* 2021. The super-relaxed state and length dependent activation in porcine myocardium. *Circ Res*. 129:617–630.

66 Touma AM, *et al.* 2022. Nanosurfer assay dissects β-cardiac myosin and myosin-binding protein C interactions. *Biophys J*. 121:2449–2460.